Variations in surface roughness of inhomogeneous underlying surfaces in the Nagqu area of the Tibetan Plateau

Maoshan Li[*1],Xiaoran Liu[2], Lei Shu[1], Lingzhi Wang[1], Wei Fu[1],Yaoming Ma [3], Yaoxian Yang[4], Fanglin Sun [4]

(1.School of Atmospheric Sciences/Plateau Atmosphere and Environment Key Laboratory of Sichuan Province/Joint Laboratory of Climate and Environment Change, Chengdu University of Information Technology, Chengdu 610225, Sichuan China;

2. Climate Center, Meteorological Bureau of Inner Mongolia Autonomous Region, Huhehot 010051, Inner Mongolia Autonomous Region, China)

3.Key Laboratory of Tibetan Environment Changes and Land Surface Processes, Institute of Tibetan Plateau Research, Chinese Academy of Sciences, CAS Center for Excellence in Tibetan Plateau Earth Sciences, Beijing, China;

3. Key Laboratory of Land Surface Process and Climate Change in Cold and Arid Regions, Chinese Academy of Sciences. Lanzhou, China)

Abstract: The temporal and spatial variation characteristics of the surface roughness in the Nagqu area of the northern Tibetan Plateau were analysed in 2008, 2010 and 2012 using MODIS satellite data and station atmospheric turbulence observation data, and the Massman retrieved model and measured average wind speed and turbulent flux of a single height ultrasonic anemometer were used to determine the aerodynamic surface roughness. The results showed that the surface roughness length has obvious seasonal variation characteristics. From February to August, $Z0m$ increased constantly with snow ablation and vegetation growth, and the maximum value reached 4-5 cm at the BJ site. From September to February, $Z0m$ gradually decreased with the post-monsoon phase over the plateau, and the values decreased to approximately 1-2 cm. Snowfall in abnormal years was the main reason for the obviously lower $Z0m$ compared with that in normal conditions. The underlying surface can be divided into four categories according to the different

---

[*] Corresponding author

Dr. Maoshan Li

Chengdu University of Information Technology

24 Block 1, Xuefu Road, Chengdu 610225, Sichuan, China

E-mail: lims@cuit.edu.cn

values of Z0m: snow and ice, sparse grassland, lush grassland and town. Among them, lush grassland and sparse grassland accounted for 62.49% and 33.74% respectively, and their Z0m annual changes are between 2-6 cm and 1-4 cm. The two methods were positively correlated with each other, and the retrieved data values were lower than the measured results due to non-uniformity of underlying surface. These results are substituted into Noah-MP replaces the original parameter design numerical simulation experiment. After replacing the model surface roughness, the sensible heat flux and laten heat flux has a better daily improvement effect.

Key words: Northern Tibetan Plateau; Surface roughness; NDVI; MODIS

1 Introduction

Known as the "third pole" of Earth (Jane, 2008), the Tibetan Plateau has an average altitude of over 4000 m and accounts for a quarter of China's territory. It is located in southwestern China adjacent to the subtropical tropics in the south, and it reaches the mid-latitudes in the north, making it the highest plateau in the world. Due to its special geographical location and geomorphic characteristics, it plays an important role in the global climate system as well as the formation, outbreak, duration and intensity of the Asian monsoon (Yang et al., 1998; Zhang et al., 1998; Wu et al., 1999, 2004, 2005; Ye et al, 1998; Wu et al, 1998; Tao et al, 1998). Many studies (Wu et al., 2013; Wang, 1999; Ma et al, 2002) have shown that the land-atmosphere interaction on the Tibetan Plateau plays an important role in the regional and global climate. Over the past 47 years, the Tibetan Plateau has shown a significant warming trend and increased precipitation (Li et al., 2010). The thermal effects of the Tibetan Plateau not only have an important impact on the Asian monsoon and precipitation variability but also affect the atmospheric circulation and climate in North America, Europe and the South Indian Ocean by inspiring large-scale teleconnections similar to the Asia-Pacific Oscillation (Zhou et al., 2009).

The various thermal and dynamic effects of the Tibetan Plateau on the atmosphere affect the free atmosphere via the atmospheric boundary layer. Therefore, it is particularly important to analyse the micrometeorological characteristics of the atmospheric boundary layer of the Tibetan Plateau, especially the near-surface layer (Li et al., 2000). Affected by the unique underlying

surface conditions of the Tibetan Plateau, local heating shows interannual and interdecadal variability (Zhou et al., 2009). Different underlying surfaces have differing diversities, complex compositions and uneven distributions and contribute to diverse and complex land surfaces. As the main input factor for atmospheric energy, the surface greatly affects the various interactions between the ground and the atmosphere and even plays a key role in local areas or specific times (Guan et al, 2009). The surface characteristic parameters (dynamic roughness, thermodynamic roughness, etc.) play an important role in the land surface process and are important factors in causing climate change (Jia et al., 2000). The underlying surface of the Tibetan Plateau presents different degrees of fluctuation, which introduces certain obstacles to understanding the land-atmosphere interaction of the Tibetan Plateau. The fluctuating surface may alter the arrangement of roughness elements on the surface and cause changes in surface roughness. Changes in roughness can also affect changes in the characteristics of other surface turbulent transportation, which may also result in changes in surface fluxes. Chen et al. (2015) presented a practical approach for determining the aerodynamic roughness length at fine temporal and spatial resolutions over the landscape by combining remote sensing and ground measurements. Surface roughness is an important parameter in land surface models and climate models. Its size reflects the matter energy exchange, transmission intensity and interactions between the near surface airflow and the underlying surface to some extent (Liu et al., 2007; Irannejad et al, 1998; Shao et al, 2000; Zhang et al., 2003). Zhou et al. (2012) demonstrated that simulated sensible heat flux compared with measurement was significantly improved by using a time-dependent Z0m parameter. Therefore, the primary objective of this study is to calculate the surface roughness and its variation characteristics to further understand the land-atmosphere interactions on the central Tibetan Plateau.

Through the study of surface roughness, it is beneficial to obtain the surface feature parameter values in the region, provide the ground truth value for model inputs, improve the simulation level of the model in the Tibetan Plateau, and deepen the understanding of the land-atmosphere interaction process. Research on model simulations of surface flux has achieved good results in many regions (Smirnova et al., 2016). Especially with the continuous development

82 and improvement of numerical models in recent years, research on the applicability of different

83 parameterization schemes in different models to different regions has continued. Luo et al. used

84 the land surface model CoLM to conduct a single-point numerical simulation of the BJ station and

85 successfully simulated the energy exchange process in the Nagqu area (Luo et al., 2009). Zhang et

86 al. evaluated the surface physical process parameterization schemes of the Noah LSM and

87 Noah-MP models in the entire East Asia region and evaluated the simulation of the surface heat

88 flux of the Tibetan Plateau (Zhang et al., 2017). Xie et al. explored the simulation effect of the

89 land surface model CLM4.5 in the alpine meadow area of the Qinghai-Tibet Plateau (Xie et al.,

90 2017). Xu et al. studied the applicability of different parameterization schemes in the WRF model

91 when simulating boundary layer characteristics in the Nagqu area (Xu, et al., 2018). Zhang, et al.

92 Comparative analyses have been performed of the meteorological elements simulated by different

93 land surface process schemes in the WRF model in the Yellow River source region (Zhang et al.,

94 2019). However, the applicability of the model in the Tibetan Plateau needs further study. The

95 terrain of the Tibetan Plateau is complex, the underlying surface is very uneven, and the area has

96 high spatial heterogeneity. Because the condition of the underlying surface has a very significant

97 impact on the surface flux, obtaining information on the surface vegetation status of a certain area

98 is very helpful for analysing the spatial representation of the surface flux.

99 In this study, satellite data are obtained by MODIS and the normalized difference vegetation

100 index (NDVI) in the Nagqu area is used to study the dynamic surface roughness length.

101 Atmospheric turbulence observation data from 2008, 2010, and 2012 and observation data from

102 automatic weather stations were collected for three observation stations in the region, and the

103 measured values of the average wind speed and turbulent flux of a single height ultrasonic

104 anemometer were used to determine the surface dynamic roughness Z0m (Chen et al., 1993). The

105 time-scale dynamics of Z0m and the results of different underlying surfaces were analysed.

106 Through a comparison of the calculation results of the observation data, we studied whether the

107 surface roughness values retrieved by satellites are reliable to provide accurate surface

108 characteristic parameters. Then we used the retrieved surface roughness to replace the surface

109 roughness in the original model for numerical simulation experiments, and evaluated the model

110 simulation results. These researches will helpful for the study of land-atmosphere interactions in

111 the plateau area and improve the theoretical research level of the near-surface layer on the Tibetan

112 Plateau. In the following section, we describe the case study area, the MODIS remote sensing data,

113 the ground observations, and the land cover map used to drive the revised Massman model

114 (Massman et al, 1997, 1999). In Section 3, we present the results and then a validation based on

115 flux measurements at Nagqu station. Finally, we provide some concluding remarks on the

116 variation characteristics of aerodynamic roughness lengths and numerical simulation of the

117 surface turbulent flux in the Nagqu area of the central Tibetan Plateau.

118

2 Study area, Data and methods

2.1 Study area and Data

121 The area selected in this study is a 200×200 km^2 area centred on the Nagqu Station of Plateau

122 Climate and Environment of the Northwest Institute of Ecology and Environmental Resources,

123 Chinese Academy of Sciences, Northern Tibet Plateau.

124 In this area, three meteorological observatory stations are located: North Pam (Portable

125 Automated Meso-net) Automatic Meteorological Observatory (NPAM), Nam Co Station for

126 Multisphere Observation and Research, Chinese Academy of Sciences (NAMC), and BJ station

127 (Figure 1). The underlying surface around the observation point is relatively flat on a small spatial

128 scale, and a certain undulation is observed at a large spatial scale. The data used included

129 observations from atmospheric turbulence and automatic meteorological stations.

130 The BJ station is located at coordinates 31.37°N, 91.90°E and an altitude of 4509 m a.s.l. The

131 BJ observation point is located in the seasonal frozen soil area, and the vegetation is alpine

132 grassland. The site measurement equipment includes an ultrasonic anemometer (CAST3,

133 Campbell, Inc.), CO_2/H_2O infrared open circuit analyser (LI 7500) and automatic meteorological

134 observation system (Ma et al., 2006). This study uses the BJ station data from 2008 and 2012. The

135 NPAM station is located at 31°56'N, 91°43'E and has an altitude of approximately 4700 m. The

136 ground of the experimental field is flat, and the area is wide. The ground is covered by a plateau

137 meadow that grows 15 cm high in summer. The experimental station observation equipment

138 includes an ultrasonic wind thermometer and humidity probe pulsator and includes data on

139 temperature and humidity, air pressure, average wind speed, average wind direction, surface

140 radiation temperature, soil heat flux, soil moisture and temperature, and radiation (Ma et al., 2006).

141 The NAMC station is located at 30°46.44'N, 90°59.31'E and an altitude of 4730 m. It is located on

142 the southeastern shore of Namco Lake in Namuqin Township, Dangxiong County, Tibet

143 Autonomous Region. It is backed by the Nyainqentanglha Mountain Range, and the underlying

144 surface is an alpine meadow. This study uses NPAM station data for the whole year of 2012 and

145 NAMC station data for the whole year of 2010.

146   **Figure 1 about here**

147   **Table 1 about here**

148   The land cover data used in this study are GLC2009 (Arino et al, 2010) data from the Envisat

149 satellite in 2009, and the spatial resolution is 300 m. The classification standard is the land cover

150 classification system (LCCS), and it divides the global surface into 23 different types, with the

151 study area including 14 of these types. The actual situation in the selected area does not match the

152 data part of GLC2009 because of the lack of an underlying surface, such as farmland, in the

153 selected area. Therefore, according to the actual land cover types obtained by Chu (Chu, 2010),

154 the categories irrigated farmland, dry farmland, mixed farmland vegetation, mixed multivegetation

155 land, closed grassland and open grassland are replaced with 6 grasslands, shrub meadows,

156 mountain meadows, alpine grasslands, alpine meadows and sparse vegetation in the mountains.

157 Since the proportion of the underlying surface of the tree as a whole is only 0.36%, the underlying

158 surface types evergreen coniferous forest, the mixed forest, the multiforest grassland mix and the

159 multigrass forestland mix will no longer be studied.

160   The MODerate-resolution Imaging Spectroradiometer (MODIS) is an important sensor on

161 board the satellites TERRA and AQUA launched by the US Earth Observing System Program. The

162 band of the MODIS sensor covers the full spectrum from visible light to thermal infrared; thus,

163 this sensor can detect surface and atmospheric conditions, such as surface temperature, surface

164 vegetation cover, atmospheric precipitation, cloud top temperature, etc. The maximum spatial

165 resolution is 250 m. The normalized vegetation index obtained by MODIS is the MYD13Q1

166 product, which provides a global resolution of 250 m per 16 days. This study selects 73 materials

167 for 2008, 2010 and 2012 in Nagqu.

168 **2.2 Methodology**

169 **2.2.1 Method for calculating surface roughness by observation data**

170 Using the measured values of the average wind speed and turbulent flux of a single height

171 ultrasonic anemometer, the calculation scheme of surface roughness proposed by Chen et al.

172 (Chen et al., 1993) was selected and the dynamic variation in the surface roughness was obtained.

173 According to the Monin-Obukhov similarity theory (Monin et al., 1954), the wind profile

174 formula with the stratification stability correction function (Panosky et al, 1984) is as follows:

175
$$U(z) = \frac{u_*}{k} \left[\ln \frac{z-d}{Z_{0m}} - \psi_m(\zeta) \right] \qquad (1)$$

176
$$\psi_m(\zeta) = 2\ln(\frac{1+x}{2}) + \ln(\frac{1+x^2}{2}) - \tan^{-1}(x) + \frac{\pi}{2} \qquad \zeta < 0 \qquad (2)$$

177
$$\psi_m(\zeta) = -5\zeta \qquad \zeta > 0 \qquad (3)$$

178 where $u_* = \sqrt{-\overline{u'w'}}$; Z0m is the dynamic surface roughness length; z is the observed height;

179 d is zero plane displacement, which is set to 0.03 m and calculated from the average vegetation

180 height 0.045 m (Stanhill, 1969); U is the average wind speed; k is the Karman constant, which is

181 set to 0.40 (Högström,1996); $L = -\dfrac{u_*^3}{(k\dfrac{g}{\theta})\overline{\theta'\omega'}}$ is the Monin-Obukhov length (Monin et al.,

182 1954); $x = (1-16\zeta)^{1/4}$; and $\zeta = (z-d)/L$ is the atmospheric stability parameter. Available

183 from formula (2.1):

184

185
$$\ln \frac{z-d}{Z_{0m}} = \frac{kU}{u_*} + \psi_m(\zeta) \qquad (4)$$

186 Using equations (2)~(4), Z0m can be determined by fitting ζ and observing a single height

187 $\dfrac{kU}{u_*}$.

2.2.2 Method for calculating surface roughness by satellite data

For a fully covered uniform canopy, Brutsaert suggested that z 0 m=0.13 hv (Brutsaert, 1982). For a canopy with proportional coverage (partial coverage), Raupach (Raupach, 1994) indicated that z 0 m/hv varies with the leaf area index (LAI). However, Pierce et al. (Pierce et al. 1992) pointed out that for all kinds of biological groups, the leaf area index can be obtained from the NDVI and the density grade of vegetation can be related to the NDVI. Asrar et al. (Asrar et al., 1992) pointed out that a mutual relationship occurred among the LAI, NDVI and ground cover through the study of physical models. Moran's study (Moran, et al., 1994) provides another method that uses the function of the relationship between NDVI and Z_{0m} in the growing season of alfalfa.

Considering that the main underlying surface of the study area is grassland, this study selects the Massman model (Massman et al, 1997, 1999) to calculate the Z0m in the Nagqu area of the central Tibetan Plateau. The Massman model is calculated as follows:

$$\gamma = C_1 - C_2 \cdot exp(-C_3 \cdot C_d \cdot LAI) \qquad (5)$$

$$n_{ec} = \frac{C_d \cdot LAI}{2 \cdot \gamma^2} \qquad (6)$$

$$d_h = 1 - \frac{[1 - exp(-2 \cdot n_{ec})]}{2 \cdot n_{ec}} \qquad (7)$$

$$\frac{Z_{0m}}{h} = [1 - d_h] \cdot exp(-\frac{k}{\gamma}) \qquad (8)$$

where C_1=0.32, C_2=0.26, and C_3=15.1 are constants in the model and related to the surface drag coefficient; LAI is the leaf area index; C_d=0.2 is the drag coefficient of the foliage elements; n_{ec} is the wind speed profile coefficient of fluctuation in the vegetation canopy; and h is the vegetation height. In many earlier studies, the high-altitude environment of the Tibetan Plateau was correlated with a low temperature in the study area and shown to affect the height and sparseness of the vegetation. Based on previous research, this study considers that the vegetation height in northern Tibet is related to the normalized differential vegetation index (NDVI) and altitude (Chen et al, 2013) and introduces the altitude correction factor on the original basis. The following is the calculation formula:

$$H = h_{min} + (\frac{h_{max} - h_{min}}{NDVI_{max} - NDVI_{min}})(NDVI - NDVI_{min}) \qquad (10)$$

214

$$h = acf \cdot H \qquad (11)$$

215

216   where h_{min} and h_{max} are the minimum and maximum vegetation height observed at the

217   observation station, respectively, $NDVI_{max}$ and $NDVI_{min}$ are the maximum and minimum NDVI of

218   the observation station, respectively; H is based on the assumption that the vegetation height is

219   directly proportional to the NDVI; x is the altitude, which is obtained from ASTER's DEM

220   products; and acf is the altitude correction factor (Chen et al., 2013), which is used to characterize

221   the effect of elevation on the height of vegetation in northern Tibet. The acf parameter has the

222   following form:

$$acf = \begin{cases} 0.149, x > 4800 \\ 11.809 - 0.0024 \cdot x, 4300 < x < 4800 \\ 1.49, x < 4300 \end{cases} \qquad (12)$$

223

224   The LAI used in this study is calculated by the NDVI of MODIS (Su,1996). The calculation

225   formula is as follows:

$$LAI = \left(\frac{NDVI * (1 + NDVI)}{1 - NDVI} \right)^{0.5} \qquad (13)$$

226

3 Results analysis

227

3.1 Variation characteristics of surface roughness based on measured data

228

229   Figure 2 shows the temporal variation characteristics of the surface roughness of sites in

230   different years in the Nagqu area. The Z0m value has continued to increase since February to

231   reach a maximum in July and August. The results for the BJ and NPAM stations in 2012 show that

232   July has slightly larger values than August, and the results for the NAMCO station in 2010 and BJ

233   station in 2008 show that August has larger than July. The BJ station may have experienced a

234   precipitation process in July 2008, resulting in a July Z0m value less than June. After August, the

235   Z0m value began to decrease, and in December, the value was approximately the same as the

236   value in January. In general, the change in the Z0m degree of each station increases from spring to

237   summer and decreases month by month from summer to winter.

239

3.2 Spatiotemporal variation characteristics of surface roughness length retrieved by MODIS data

242   Figure 3 shows a plot of the surface roughness distribution of 200×200 km^2 around the BJ

243   site in 2008. In February, the Z0m decreased from January, which may have been due to snowfall,

244   temperature, etc., resulting in a small Z0m that continued to decrease. Due to the rising

245   temperature and snow melting, Z0m showed a slowly increasing trend from February to May and

246   a rapid increase from June to August. From June onwards, a large number of surface textures were

247   observed, indicating the complexity of the underlying surface. Whether the bulk surface or

248   vegetation had a more important impact on Z0m is not clear. From May to August, obvious

249   changes in humidity, temperature and pressure caused by the plateau summer monsoon led to an

250   increase in the height and coverage of surface vegetation, and Z0m peaked in August. In particular,

251   the change from May to June was very significant, which may have been related to the beginning

252   of the summer monsoon in June, the corresponding increase in precipitation, theaccelerated the

253   growth of vegetation and the rapid rise of Z0m. In June, July, and August, continuous precipitation

254   and rising temperatures led to vigorous vegetation growth, although changes were not observed

255   after the vegetation reached maturity. The corresponding maximum value of Z0m in the figure

256   remains unchanged, although due to sufficient values in these three months, the area with high

257   Z0m values gradually expanded and reached the maximum range in August. From September to

258   December, as the plateau summer monsoon retreated, the temperature and humidity gradually

259   decreased. Compared with the plateau summer monsoon, the conditions were no longer suitable

260   for vegetation growth; thus, the contribution of vegetation to Z0m was weakened, the surface

261   vegetation height gradually decreased, and Z0m continued to decrease. Moreover, the range of

262   large-value regions also gradually decreased.

263   **Figure 3 about here**

264   **Figure 4 about here**

265   Figures 4 and 5 show the retrieved monthly surface roughness values in the BJ area in 2010

266   and 2012, respectively. Moreover, Z0m also showed a decrease from January to February in the

267 Nagqu area in 2010 and 2012. Starting in February, Z0m increased. Starting in June, Z0m

268 increased rapidly and reached the peak of the whole year in August. Subsequently, Z0m began to

269 decrease.

270 **Figure 5 about here**

271   Figures 3, 4, and 5 show that Z0m changes with the spatial and temporal scale. Z0m shows

272 different trends on different underlying surfaces. In November 2008, the Z0m in the Nagqu area

273 was small overall and generally as low as 1 cm. Historical data show that there is a large-scale

274 snowfall process in the Nagqu area at this time. Snowfall over the meadow causes the underlying

275 surface of the meadow to be homogeneous and flat, and after the snowfall falls, it is easy to form a

276 block with a scattered and discontinuous underlying surface. We subsequently determined that the

277 surface roughness of the area with ice and snow as the underlying surface is not more than 1 cm,

278 which is consistent with historical weather processes. Therefore, we think that snowfall caused the

279 Z0m in November to be very small. From November to December, Z0m showed a growing trend,

280 which may be due to temperature, unfrozen soil or other reasons that resulted in the melting of

281 snow, and then the surface roughness showed a growing trend (Zhou, 2017).

282 **3.3 Evaluation of satellite data retrieved results**

283 **Figure 6 about here**

284   The underlying surfaces of the three sites selected in this study are all alpine meadows. In

285 Figure 6, the NPAM site data calculation results are larger than the satellite data retrieved results

286 throughout the year. Only the values in September and October are very close, and the trends are

287 similar. The maximum value of the site data calculation is 5 cm and the satellite data retrieved

288 result is 4.5 cm. The maximum difference is in May at 1.7 cm. The NAMCO station data

289 calculation results are very close to the satellite data retrieved results from April to November,

290 although the satellite data retrieved results are significantly larger than the site data calculation

291 results in January, March and December. The largest difference occurs in January, and the

292 difference value reaches 1.5 cm. In 2008, the calculation results of the BJ station data were larger

293 than the satellite data retrieved results throughout the year. The calculation results of the site data

294 were very close to the satellite data retrieved results from January to April and July to November,

295 although a large difference was observed in May, June and December, with the largest difference

296 occurring in May at 1.8 cm. In 2012, the BJ site data calculation results were consistent with the

297 satellite data retrieved results for the whole year, although the site data calculation results were

298 larger than the satellite data retrieved results from March to June, and the station data calculation

299 results were smaller than the satellite data retrieved at other times. As a result, the largest

300 difference occurred in June at 1.1 cm. Figure 6 shows that for the overall situation, the seasonal

301 variation trend of the site data calculation results is consistent with the satellite data retrieved

302 results in January, February, March, November and December. However, the site data calculation

303 results from April to October are greater than the satellite data retrieved results. From Figure 6, the

304 Z_{0m} calculated from the site observation data is larger than that of the satellite data, which may be

305 because of the average smoothing effect. From February to July, the single point Z_{0m} value was

306 significantly increased according to the independent method of determining the surface roughness,

307 while the results obtained by using the satellite data did not increase significantly. The satellite

308 results show that the values from January to May, November, and December are basically stable

309 below 2 cm and only change from June to October, which is related to non-uniformity of

310 underlying surface in Massman mode. In general, the results calculated by the station are generally

311 larger than those obtained by satellite retrieval.

312   Figure 7 about here

313   The Z_{0m} scatter plot is shown in Figure 7. A significant positive correlation is observed

314 between the satellite retrieval and the surface roughness calculated from the site data. The

315 correlation coefficients between the observation result and the retrieved result are large except for

316 at the NAMCO station in 2010 in Figure 7(g). The average result of the underlying surface were

317 consistent with the underlying surface results in different regions, further indicating that the

318 satellite retrieved results are consistent with the site calculation results. However, the results of the

319 NAMCO site are different from those of the other sites. The correlation coefficient with the

320 average results of the underlying surface is 0.83, and the correlation coefficient with the satellite

321 retrieved results is 0.62. Because the Namco Observation Station is closer to the lake (1 km), it is

322 more affected by local microclimates, such as lake and land winds. The results in Figure 7 all

323 passed the F test of P=0.05, which indicates that there is no significant difference between the site

324 data calculation results and the satellite data retrieved results.

4 Variation characteristics of the surface roughness of different underlying surfaces

According to the vegetation dataset GLC2009 combined with actual local conditions, the 200×200 km^2 area of Nagqu was divided into 10 different underlying surfaces (Arino et al., 2010): mountain grassland, shrub meadow, mountain meadow, alpine grasslands, alpine meadows, sparse vegetation lap, urban land, bare land, water bodies, ice sheets and snow cover.

Figure 8 about here

The monthly variation in Z0m in different underlying surfaces in the Nagqu area is shown in Figure 8, which indicates that 14 different underlying surfaces in the Nagqu area can be divided into four categories. The first category is urban land, which accounts for 0.07% of the whole study area. The Z0m of this type of underlying surface is greater than that of other types throughout the year, and the change in Z0m is very large, which is probably due to the irregular changes in the underground areas of the selected areas and the irregularities caused by human activities. The second category is lush grassland, including shrub meadows, mountain grasslands, alpine grasslands and mountain meadows, which account for 62.49% of the area. The variation curves of Z0m of the four underlying surfaces are similar, and the Z0m of the urban land is only smaller than that of other underlying surfaces. The third category is sparse grassland, including alpine sparse vegetation, alpine meadows and bare land, and it accounts for 33.74% of the area. The Z0m values of the three underlying surfaces are similar at a medium height. The Z0m of the bare soil is at the lowest point of these underlying surface Z0m, and the Z0m of the alpine meadow is relatively stable and less affected by the outside. The fourth category is ice and snow, including ice sheets and snow cover, and water bodies are two kinds of underlying surfaces, accounting for 3.7% of the area. The Z0m of these three underlying surfaces presents another phenomenon. The variation range of the whole year is relatively small, and the Z0m of these underlying surfaces is also small. It is more than 1 cm in mid-June and less than 1 cm at other times. Figure 8(d) shows the multiyear average seasonal variation in Z0m. The figure clearly shows that the underlying surface can be divided into four categories due to the difference in surface roughness. The change from January to May Z0m is very small, peaking from May to August and then down to the

previous January to May level in November and December. The snowfall in November 2008 may

have led to the low level of November in Figure 8(d). Table 2 shows that the winter albedo at the

BJ station and Namco station is higher than that in other seasons, and the summer is the smallest.

Both show that the surface albedo in November 2008 was significantly higher than that in

November of the other two years. In fact, the surface roughness on November should be higher

than that on December in former years.

Table 2 about here

Figure 8 also shows that in the Nagqu area, except for the area of the fourth type of

underlying surface, the Z0m change in other areas decreases from January to February and begins

to increase after February, reaching a peak in August and then starting to decrease. However,

Figure 6 clearly shows that there are several stages in which Z0m changes significantly, in early

April, mid-May, early July, late August, and late September. The change at the end of August was

the most obvious. Each of the underlying surfaces Z0m changes by more than 2 cm on average.

The extent of the change in late September was also large, with an average change of more than

1.5 cm. Moreover, the change in early July was special because the change resulted in a significant

increase in the Z0m of water bodies and ice.

Certain factors, such as cloud cover in May, August, and November of 2008; August and

September of 2010; and April and July of 2012, caused significant changes in the overall Z0,

which resulted in two very significant changes in the three-year average for August and November.

In November, the change was caused by snowfall based on other meteorological data. In August

2008 and 2010, the changes was caused by precipitation based on an analysis of the sudden

increase in the Z0m of the water body and ice and snow surface. Combined with several changes

in Z0m, precipitation, snowfall, and snow accumulation will make the underlying surface more

uniform and flatter, which will lead to relative reductions in Z0m.

5 Simulation and evaluation of Noah-MP model

5.1 Model setup

According to the surface roughness variation characteristics retrieved from

satellite data, the underlying surface of Nagqu area can be divided into four types.

They are urban, lush grass, sparse grass, and ice and snow. Among them, urban accounts for 0.07%, its Z0m up to 9 cm, lush grassland accounts for 62.49% of the area, its Z0m can reach up to 6cm, sparse grassland up to 33.74%, its Z0m can reach up to about 4cm, ice and snow accounts for 3.7% of the area, and Z0m does not exceed 1cm. These results are substituted into Noah- MP replaces the original parameter design numerical simulation experiment. The model after replacing the surface roughness is set as a sensitivity experiment, and the original model is set as a control experiment. The selection of other parameterization schemes suitable for numerical simulation in Nagqu area is shown in Table 3. The simulation time is from July 1 to 31, 2008, and the spin-up time is 9 days. The forcing field dataset is a Chinese meteorological forcing dataset jointly developed by the Tibetan Plateau Data Assimilation and Modelling Centre and the Institute of Tibetan Plateau Research of the Chinese Academy of Sciences (ITPCAS).

5.2 Evaluation of the simulated single point heat flux

Figure 9(a) shows that the sensible heat flux simulated by the sensitivity experiment is closer to the measured value than the control experiment. In the daytime, the results of sensitivity experiment were smaller than those of the control experiment, and some time were larger than those of the control experiment. At night, the results of the two models were close to each other before July 21, and the sensitivity experiment results were significantly improved after July 21. Figure 9(b) shows that the sensitivity experiment results are basically consistent with the control experiment results, which are maintained at about $0W/m^2$, and there is no improvement at night. Before July 19, the two experiments latent heat fluxes remained at about $200W/m^2$, which was less than the observed latent heat flux, and the simulated maximum value of the sensitivity experiment was greater than that of the control experiment. After July 19, the two experiments simulation results began to increase and reached about $400 W/m^2$ consistent with the observed latent heat flux, indicating that the simulation effect was improved to some extent. Similarly, it can be found from the maximum

410   value that the sensitivity experiment results were slightly greater than the control

411   experiment results. It also shows that improving the accuracy of surface roughness

412   can improve the simulation effect of latent heat flux.

413   **Figure 9 about here**

414   **5.3 Evaluation of regional heat flux simulation results**

415   In order to compare the changes of sensible heat flux and latent heat flux before

416   and after improvement, the sensitivity simulations are used to subtract the control

417   model simulation results. By subtracting the sensible heat flux from control and

418   sensitivity experiment, the results are shown in the figure 10. It can also be seen from

419   the figure 10 (a) that the difference of sensible heat flux is basically negative in the

420   daytime, indicating that the sensible heat flux after improvement is smaller than that

421   before improvement. The above results show that the modified surface roughness can

422   improve the simulation effect of sensible heat flux in daytime. The results in the

423   figure 10 (c) are basically positive in the daytime, indicating that the latent heat flux

424   after improvement is larger than that before improvement, about $15W/m^2$. The above

425   results show that the model simulation results are generally less than the actual

426   observation results, so it can be considered that the improvement of surface roughness

427   in the daytime can improve the simulation of the model. Figure 10 also shows that the

428   improvement of nighttime latent heat flux is not significant, which is basically

429   maintained at $0W/m^2$.

430   Figure 10 about here

431 **6 Conclusions and discussion**

432   Through the calculation and analysis of the surface roughness of the Nagqu area in the

433   central Tibetan Plateau and comparing the retrieved satellite data with the calculation results of the

434   observational data, the attained main conclusions are as follows.

435   (1) The retrieved results of the satellite data are basically consistent with the calculated

436   results of the measured data. Both results indicate that the surface roughness continued to increase

437   from February to August, began to decrease after reaching a peak in August and reached the

lowest value in February of the following year. A strong connection is observed between the monthly variation in surface roughness and the changes in meteorological elements brought by the plateau summer monsoon. Among them, the satellite surface retrieval results in a slow increase in surface roughness from February to May.

(2) Through the characteristics of surface roughness variation retrieved by satellite data, the underlying surface can be divided into four categories according to the surface roughness (from large to small: urban, lush grassland, sparse grassland and ice and snow. Among them, lush grassland accounts for 62.49%, and the Z_{0m} can reach 6 cm; sparse grassland accounts for 33.74%, and the Z_{0m} can reach up to 4 cm; and ice and snow account for 3.7%, and the Z_{0m} does not exceed 1 cm.

(3) Comparing the results of the satellite retrieved calculations, satellite retrieved results and measured data shows that the results are positively correlated and the satellite retrieved results are better fit with the measured results. Due to the average sliding effect of the retrieved data, the satellite retrieved data are smaller than the measured results. This method can be used to calculate the surface roughness results for a region and provide a true value for the model for simulation.

(4) The accuracy of ground-air flux simulation can be improved after adjusting the surface roughness in Nagqu area. After replacing the model surface roughness, the sensible heat flux has a better daily improvement effect, about $20 W/m^2$. The night improvement effect is poor, about $0.15 W/m^2$. The improvement of latent heat flux is not obvious, and there is an improvement within $15 W/m^2$ during the daytime.

This study uses remote sensing images and an aerodynamic roughness remote sensing retrieved model to estimate the spatial scale of aerodynamic roughness conditions in northern Tibet, and this method will provide parameter and parameterization scheme improvements for model simulations to study the spatial distribution of the surface flux in the Tibetan Plateau. Air thermodynamics surface roughness is affected by shortwave and longwave radiation (the latter for deriving surface temperature), air temperature, wind speed, precipitation or snowfall. The relationship between air thermodynamics surface roughness and them and how to parameterization them in Massman mode will be studied in the future.

Acknowledgements:

This work was financially supported by the Second Tibetan Plateau Scientific Expedition and Research (STEP) program (Grant No. 2019QZKK0103), the National Natural Science Foundation of China (Grant No. 41675106,41805009) and National key research and development program of China (2017YFC1505702)

References:

Arino O, Ramos J, Kalogirou V, et al."Glob Cover 2009"[R].Edinburgh, UK:Proceedings of the living planet Symposium, 2010.

Asrar , G ., Myneni , R.B.and Chaudhury , B.J., 1992, Spatial heterogeneity in vegetation canopies and remote sensing of observed photosynthetically active radiation:a modeling study , Ren.Sens.Env ., 41, 85～103.

Brutsaert , W.A ., 1982, Evaporation into the Atmosphere , Dordrecht in Holland , D .Reidel Publishing Company,113 ～ 121.

Chu D., Basabta S., Wang W., et al, 2010. Land Cover Mapping in the Tibet Plateau Using MODIS Imagery[J]. Resources Science, 32(11): 2152-2159. (in Chinese with English abstract)

Chen, J., Wang, J., Mitsuaki, H., 1993. An independent method to determine the surface roughness length. Chin. J. Atmos. Sci. 1993, 17, 21–26. (in Chinese with English abstract)

Chen Q., L. Jia, R. Hutjes, M. Menenti, 2015, Estimation of Aerodynamic Roughness Length over Oasis in the Heihe River Basin by Utilizing Remote Sensing and Ground Data, Remote Sensing, 2015, 7(4), 3690-3709; doi:10.3390/rs70403690.

Chen X., et al, 2013. An improvement of roughness height parameterization of the Surface Energy Balance System (SEBS) over the Tibetan Plateau[J]. Journal of Applied Meteorology and Climatology, 52(3): 607-622.

Guan X., Huang J., et al, 2009. Variability of soil moisture and its relationship with surface albedo and soil thermal parameters over the Loess Plateau[J]. Advances in Atmospheric Sciences, 26(4): 692-700, doi: 10.1007/s00376-009-8198-0.

Högström U., 1996 'Review of Some Characteristics of the Atmospheric Surface Layer'

494 Boundary-Layer Meteorol 78 215–246 10.1007/BF00120937

495 Irannejad P, Shao Y P, 1998. Description and validation of the atmosphere-land-surface interaction

496 scheme(ALSIS)with HAPEX and Cabauw data[J]. Global Planet Change, 19(1): 87-114.

497 Jane Q., 2008. The third pole[J]. Nature, 454(24): 393-396.

498 Jia L., Wang J., Hu Z., 2000. The Characteristics of Roughness Length for Heat and Its Influence

499 on Determination of Sensible Heat Flux in Arid Zone[J]. Plateau Meteorology, 19(04): 495-503.

500 (in Chinese with English abstract)

501 Li F., Li S., Chen T., 2004. A Study on Develpoment of the Tibetan North Grasslands Tourism

502 Stockbreeding in Naqv Tibet[J]. Sichuan Caoyuan, 109(12): 38-42. (in Chinese with English

503 abstract)

504 Li J., Hong Z., Sun S., 2000. An Observational Experiment on the Atmospheric Boundary Layer in

505 Gerze Area of the Tibetan Plateau[J]. Chinese Journal of Atmospheric Sciences, 24(03): 301-312.

506 (in Chinese with English abstract)

507 Li L., Chen X., Wang Z., et al, 2010. Climate Change and Its Regional Differences over the

508 Tibetan Plateau[J]. Advances in Climate Change Research, 6(03): 181-186. (in Chinese with

509 English abstract)

510 Liu J., Zhou M., Hu Y., 2007. Discussion on the Terrain Aerodynamic Roughness[J]. Ecology and

511 Environment, 16(06): 1829-1836. (in Chinese with English abstract)

512 Luo S., Lü S., Yu Z. (2009) Development and validation of the frozen soil parameterization

513 scheme in Common Land Model. Cold Reg Sci Technol 55:130–140

514 Ma Y., Tsukamoto O, Wang J., et al, 2002. Analysis of aerodynamic and thermodynamic

515 parameters on the grassy marshland surface of Tibetan Plateau[J]. Progress in Natural Science,

516 12(1): 36-40.

517 Ma Y., Wang J., et al, 2002. Analysis of Aerodynamic and Thermodynamic Parameters on the

518 Grassy Marshland Surface of Tibetan Plateau[J]. Peogress in Natural Science, 12(01): 36-40. (in

519 Chinese with English abstract)

520 Ma Y., Yao T., Wang J., et al, 2006. The Study on the Land Surface Heat Fluxes over

521 Heterogeneous Landscape of the Tibetan Plateau[J]. Advances in Earth Science, 21(12):

522 1215-1223. (in Chinese with English abstract)

523 Massman W., 1997. An analytical one-dimensional model of momentum transfer by vegetation of

524 arbitrary structure[J]. Boundary-Layer Meteorology, 83(3): 407-421.

525 Massman W., 1999. An analytical one-dimensional second-order closure model of turbulence

526 statistics and the Lagrangian time scale within and above plant canopies of arbitrary structure[J].

527 Boundary-Layer Meteorology, 91(1): 81-107.

528 Monin A., Obukhov A., 1954. Basic laws of turbulent mixing in the atmosphere near the ground[J].

529 Tr Akad Nauk SSSR Geofiz Inst, 24(15): 163-187.

530 Moran, M .S ., Clarke , T .H., Inone, Y.et al., 1994, Estimating crop water deficit using the relation

531 between surface-air temperature and spectral vegetation index, Rem .Sens. of Env ., 49 , 246 ～

532 263.

533 Panosky H., Dutton J., 1984. Atmospheric Turbulence: Models and Methods for Engineering

534 Applications[M]. New York: John Wiley, 1-399.

535 Pierce , L.L., Walker, J., Downling , T .I.et al., 1992, Ecological change in the Murry -Darling

536 Basin-III :A simulation of regional hydrological changes , Journal of Applied Ecology , 30, 283～

537 294.

538 Raupach, M .R., 1994, Simplified expressions for vegetation roughness leng h and zero-plane

539 displacement as functions of canopy height and area index , Boundary -Layer Meteor ., 71, 211-

540 216.

541 Shao Y., 2000. Phtsics and Modeling of Wind Erosion[M]. London: Kluwer Academic Publishers,

542 1-452.

543 Smirnova T., Brown J., Benjamin S., Kenyon J. (2016) Modifications to the rapid update cycle

544 land surface model (RUC LSM) available in the weather research and forecasting (WRF) model.

545 Mon Weather Rev 144(5):1851–1865

546 Stanhill G., 1969. A simple instrument for the field measurement of turbulent diffusion flux. J

547 Appl Meteorol 8:509–513

548 Stull B R, 1991. An Introduction to Boundary Layer Meteorology[M]. Beijing: China

549 Meteorological Press, 1-737.

550   Su, Z., 1996. Remote Sensing Applied to Hydrology: The Sauer River Basin Study.

551   RuhrUniversität Bochum, Lehrstuhl für Hydrologie, Wasserwirtschaft und Umwelttechnik.

552   Tao S., Chen, L., Xu X., et al, 1998. Progresses of the Theoretical Study in the Second Tibetan

553   Plateau Experiment of Atmospheric Sciences (PartI)[M]. Beijing: China Meteorological Press,

554   1-348.

555   Wu G., Mao J., Duan, A., et al., 2004. Recent progress in the study on the impact of Tibetan

556   Plateau on Asian summer climate[J]. Acta Meteorologica Sinica, 62(5): 528-540. (in Chinese with

557   English abstract)

558   Wu G., Zhang Y., 1998. Tibetan Plateau forcing and timing of the Mon-soon onset over south Asia

559   and the south China sea[J]. Monthly Weather Review, 4(126): 913-927.

560   Wu G., Zhang Y., 1999. Thermal and Mechanical Forcing of the Tibetan Plateau and Asian

561   Monsoon Onset.Part Ⅱ:Timing of the Onset[J]. Chinese Journal of Atmospheric Sciences,

562   23(01): 52-62. (in Chinese with English abstract)

563   Wu G., Liu Y., Liu X., et al. 2005. How the heating over the Tibetan Plateau affects the Asian

564   climate in summer[J]. Chinese Journal of Atmospheric Sciences, 29(1): 47-56. (in Chinese with

565   English abstract)

566   Wu X., Ma W., Ma Y., 2013. Observation and Simulation Analyses on Characteristics of Land

567   Surface Heat Flux in Noethern TibetanPlateau in Summer[J]. Plateau Meteorology, 32(05):

568   1246-1252. (in Chinese with English abstract)

569   Xie Z., Hu Z., Liu H., Sun G., et al., 2017 Evaluation of the Surface Energy Exchange Simulations

570   of Land Surface Model CLM4.5 in Alpine Meadow over the Qinghai-Xizang Plateau. Plateau

571   Meteorology, 36(1): 1-12. (in Chinese with English abstract)

572   Xu L., Liu H., Xu X., et al. 2018, Applicability of WRF model to the simulation of atmospheric

573   boundary layer in Nagqu area of Tibetan Plateau[J]. Acta Meteorologica Sinica, 2018(6):955-967.

574   (in Chinese with English abstract)

575   Yang M., Yao T., 1998. A Review of the Study on the Impact of Snow Cover in the Tibetan

576   Plateau on Asian Monsoon[J]. Journal of Glaciology and Geocrylolgy, 20(2): 90-95. (in Chinese

577   with English abstract)

578 Ye D., Wu G., 1998. The role of heat source of the Tibetan Plateau in the general circulation[J].

579 Meteorological and Atmospheric Physics, 67(1): 181-198.

580 Zhang G., Zhou G., Chen F. 2017, Analysis of Parameter Sensitivity on Surface Heat Exchange in

581 the Noah Land Surface Model at a Temperate Desert Steppe Site in China[J]. Acta Meteorologica

582 Sinica. (6).1167-1182.doi:10.1007/s13351-017-7050-1.

583 Zhang Q., Lv S., 2003. The Determination of Roughness Length over City Surface[J]. Plateau

584 Meteorology, 22(01): 24-32. (in Chinese with English abstract)

585 Zhang Y., Wu G., 1998. Diasnostic Investigations of Mechanism of Onset of Asian Summer

586 Monsoon and Abrupt Seasonal Transitions Over Northern Hemisphere PartI[J]. Acta

587 Meteorologica Sinica, 56(5): 2-17. (in Chinese with English abstract)

588 Zhou X., Zhao P., Chen J., et al, 2009. Impacts of Thermodynamic Processes over the Tibetan

589 Plateau on the Northern Hemispheric Climate[J]. Sci China Ser D-Earth Sci, 39(11): 1473-1486.

590 (in Chinese with English abstract)

591 Zhou, Y., Ju, W., Sun, X., Wen, X., Guan, D. 2012 Significant decrease of uncertainties in sensible

592 heat flux simulation using temporally variable aerodynamic roughness in two typical forest

593 ecosystems of China. J. Appl. Meteorol. Climatol. 2012, 51, 1099–1110.

594 Zhou Y., Xu W., Bai A., et al, 2017. Dynamic Snow-melting Process and its Relationship with Air

595 Temperature in Tuotuohe, TibetanPlateau[J]. Plateau Meteorology, 36(1): 24-32. (in Chinese with

596 English abstract)

597

598 Figure captions

599 Fig. 1 Location of sites and the land cover on the northern Tibetan Plateau. The black solid circle

600 '●' indicates the location of the sites

601 Fig. 2 Surface roughness length of different sites on the northern Tibetan Plateau

602 Fig. 3 Surface roughness length on the northern Tibetan Plateau in 2008

603 Fig. 4 Surface roughness length on the northern Tibetan Plateau in 2010

604 Fig. 5 Surface roughness length on the northern Tibetan Plateau in 2012

605 Fig. 6 Comparison of the surface roughness length by site observations and satellite remote sense

606   retrieved data

607   Fig. 7 Scatter plots of the retrieved and calculated surface roughness lengths at four sites

608   Fig. 8 Curve of the surface roughness length for different underlying surfaces
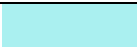
609   Fig.9 Comparison of simulated and observed sensible heat flux (a) and Comparison of simulated

610   and observed latent heat flux (b)

611   Fig. 10 The difference of the control and sensitivity experiments simulated regional sensible heat

612   flux (a) 12:00, (b) 00:00 and latent heat flux (c) 12:00, (d) 00:00

613

614   Tables

615   Table 1. Legend of the land cover map on the northern Tibetan Plateau

Value	Colour	Land Cover Types	Percent (%)
11		Mountain grassland	5.79
14		Shrub meadow	3.25
20		Mountain meadow	8.26
30		Alpine grassland	45.16
70		Needle-leaved evergreen forest	0.23
100		Mixed forest	0.03
110		Mixed forestland and grassland	0.06

616

Value	Colour	Land Cover Types	Percent (%)
120		Mixed grassland and	0.04
140		Alpine meadow	28.28
150		Alpine sparse vegetation	0.29
190		Urban areas	0.07
200		Bare areas	4.90
210		Water bodies	2.57
220		Permanent snow and ice	1.07

617

618

619

620

621

 Table 2 the observed albedo of the sites (BJ and Namco) on the northern Tibetan

 Plateau

Site	year	Jan.	Feb.	Mar.	Apr.	May.	Jun.	Jul.	Aug.	Sep.	Oct.	Nov.	Dec.
BJ	2008	0.13	0.17	0.14	0.13	0.12	0.10	0.09	0.09	0.09	0.16	**0.32**	0.16
	2009	0.30	0.26	0.30	0.25	0.26	0.21	0.19	0.19	0.21	0.26	0.24	0.26
	2010	0.26	0.30	0.31	0.30	0.34	0.22	0.19	0.18	0.18	0.35	0.26	0.27
NAMCO	2008	0.28	0.28	0.31	0.28	0.25	0.21	0.17	0.18	0.18	0.30	**0.89**	0.28
	2009	0.35	0.32	0.28	0.24	0.26	0.22	0.19	0.17	0.22	0.24	0.31	0.27
	2010	0.45	0.23	0.25	0.24	0.29	0.22	0.20	0.17	0.18	0.40	0.35	0.24

624

625

626

627

628

629

630

631

632

633 Table 3 The selected other schemes in Noah-MP

Options for different schemes	Name of the option
dynamic vegetation	Use table LAI; use FVEG=SHDFAC from input
canopy stomatal resistance	Ball-Berry's method
soil moisture factor for stomatal resistance	Noah's method
runoff and groundwater	TOPMODEL with groundwater
surface layer drag coeff	Monin-Obukhov's method
supercooled liquid water	No iteration
frozen soil permeability	Nonlinear effects, less permeable
radiation transfer	Two-stream applied to grid-cell
ground snow surface albedo	Classic method
partitioning precipitation into rainfall & snowfall	Jordan's method
lower boundary condition of soil temperature	TBOT at ZBOT (8m) read from a file
snow/soil temperature time scheme	full implicit (original Noah); temperature top boundary condition

634

635
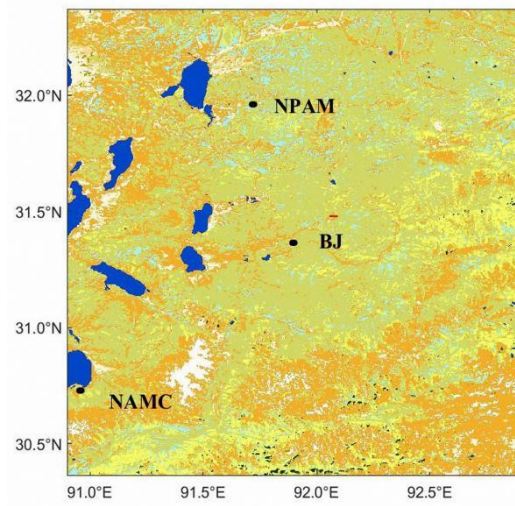
636

637   Fig. 1 Location of the sites and the land cover on the northern Tibetan Plateau. The black solid

638   circle '●' indicates the location of the sites.

639
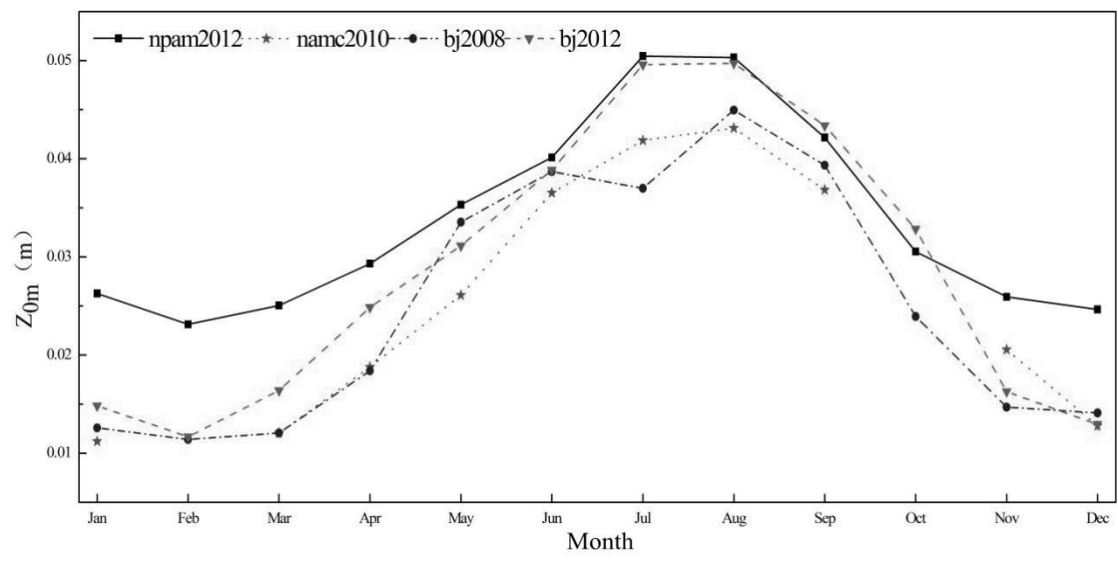
640

641   Fig. 2 Surface roughness length of different sites on the northern Tibetan Plateau

642

643

644

645
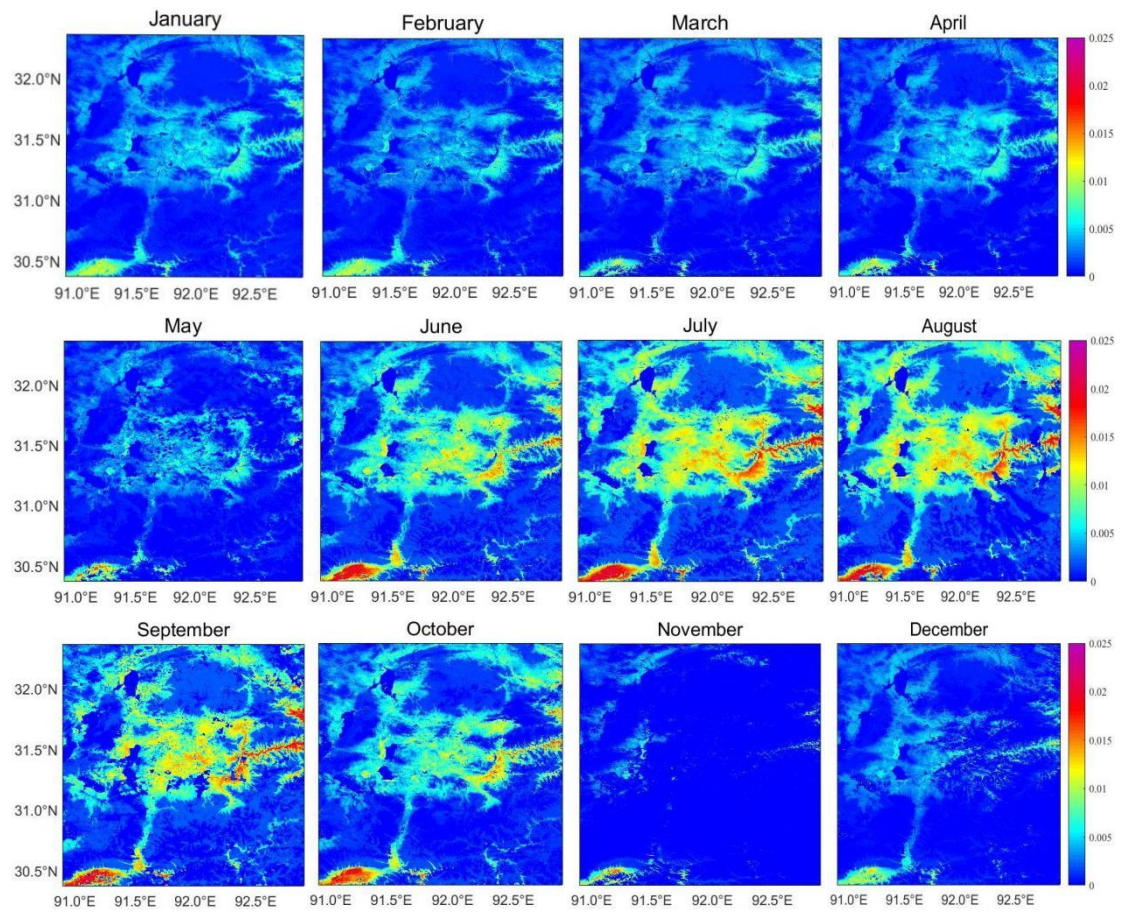
Fig. 3 Surface roughness length on the northern Tibetan Plateau in 2008

646

647

648

649

650

651
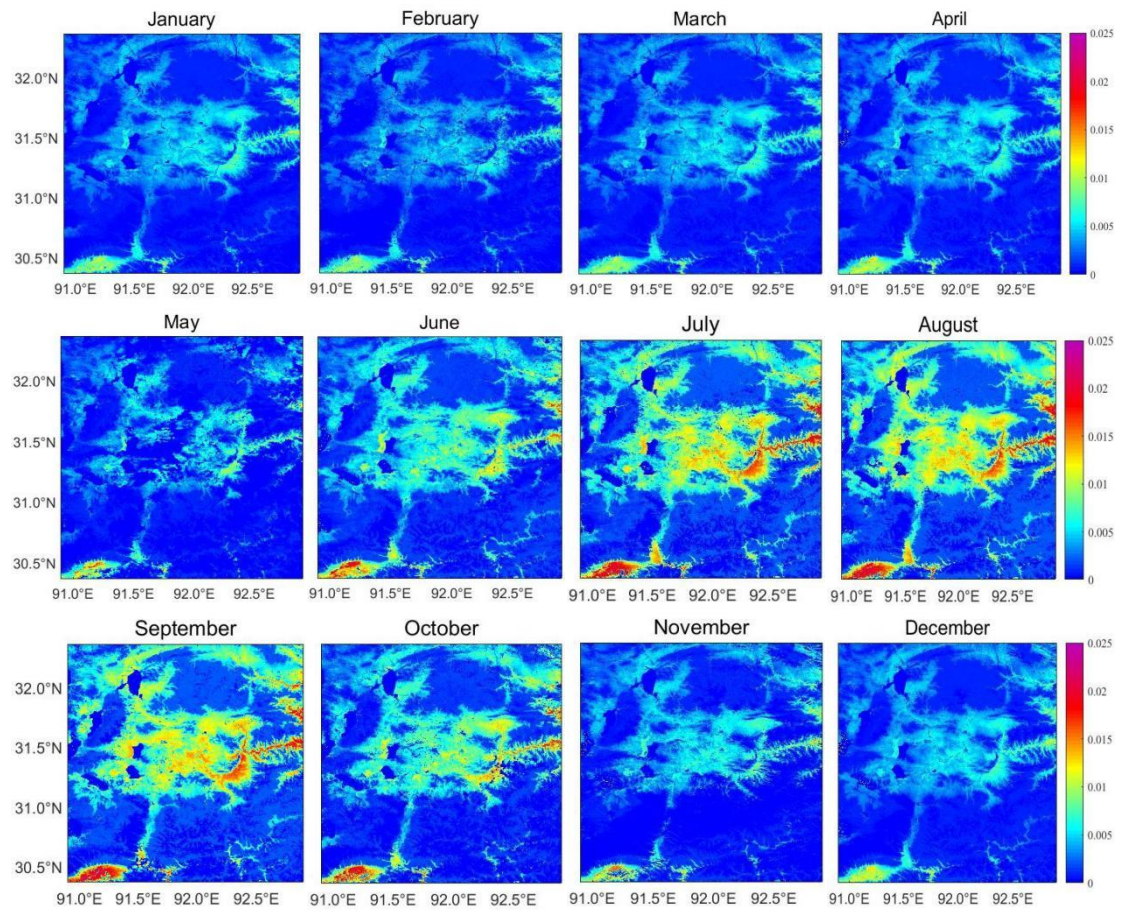
Fig. 4 Surface roughness length on the northern Tibetan Plateau in 2010

653

654
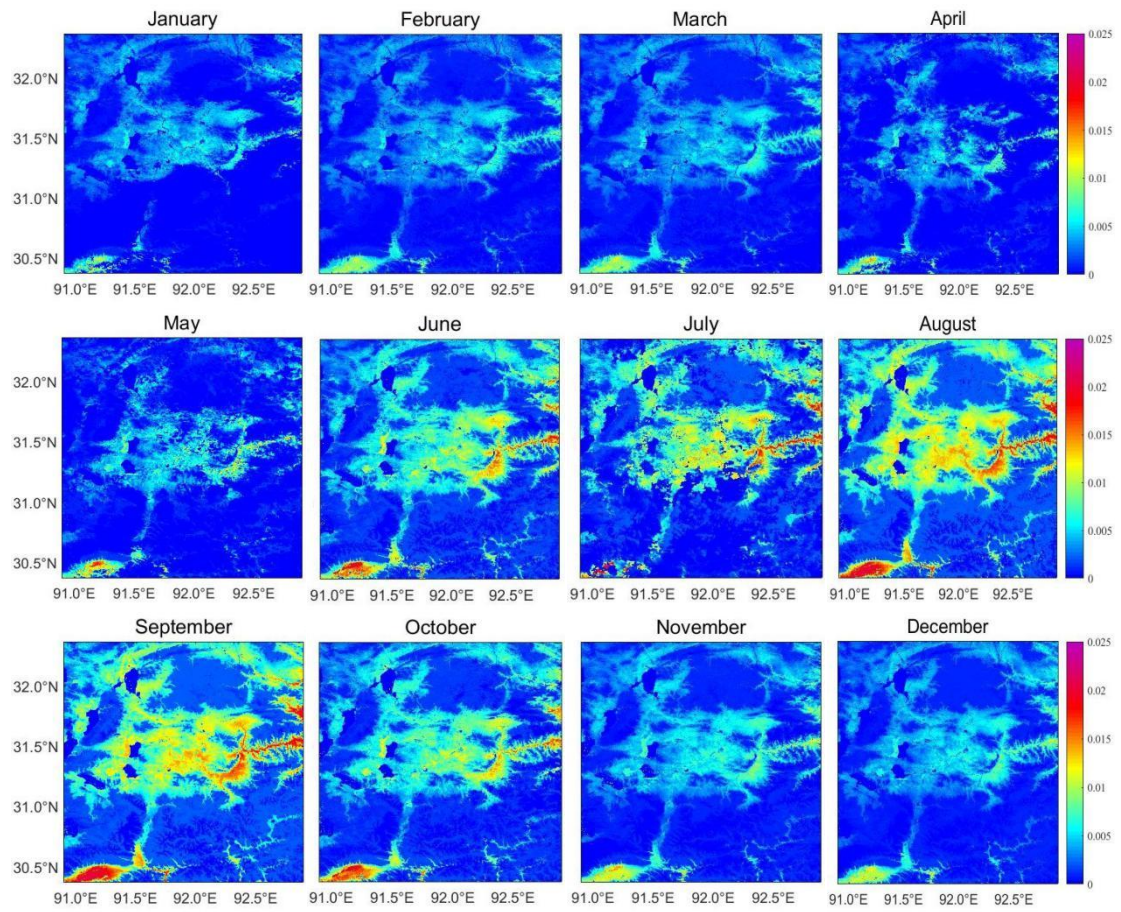
655

656

657

Fig. 5 Surface roughness length on the northern Tibetan Plateau in 2012

658

659
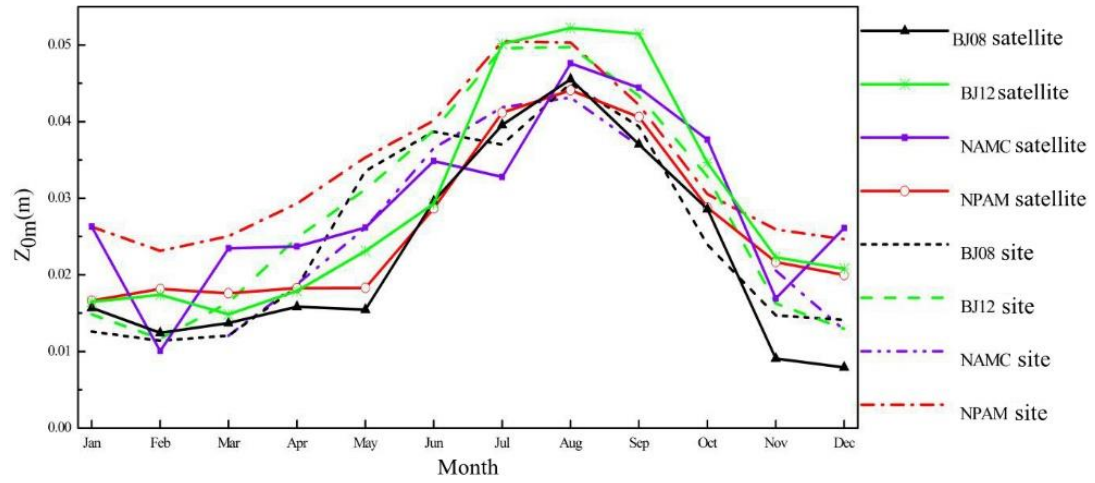
660

661   Fig. 6 Comparison of the surface roughness length by site observations and satellite remote sense

662   retrieved data

663
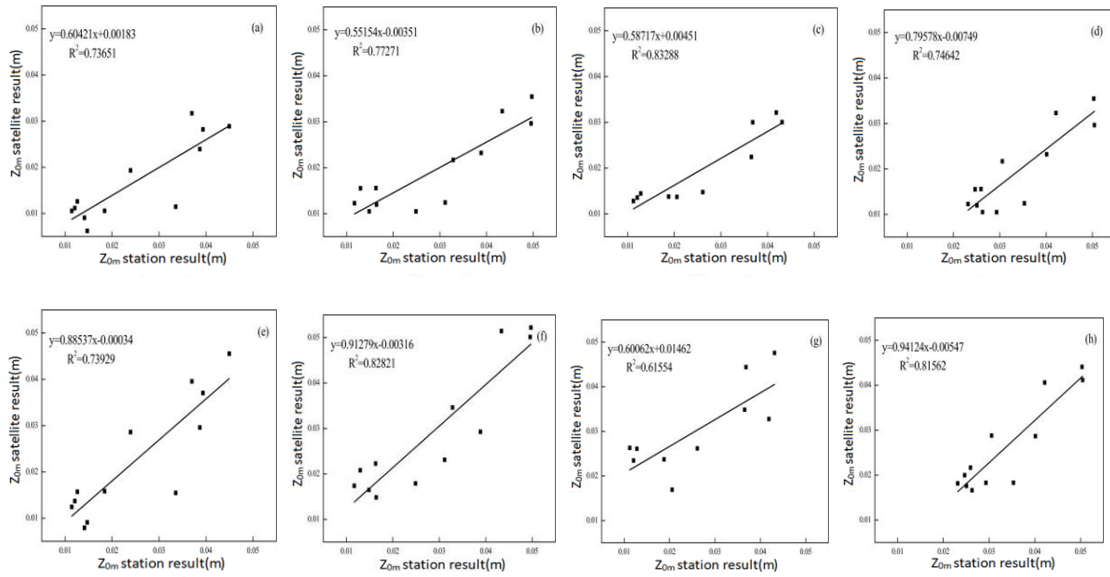
Fig. 7 Scatter plots of the retrieved and calculated surface roughness lengths at four sites

(a-d: scatter plot of the observation results and the average result of the underlying surface; e-h:

scatter plot of the observation and retrieved results; a, e: BJ station in 2008; b, f: BJ station in

2012; c, g: NAMC station in 2010; and d, h: NPAM station in 2012)
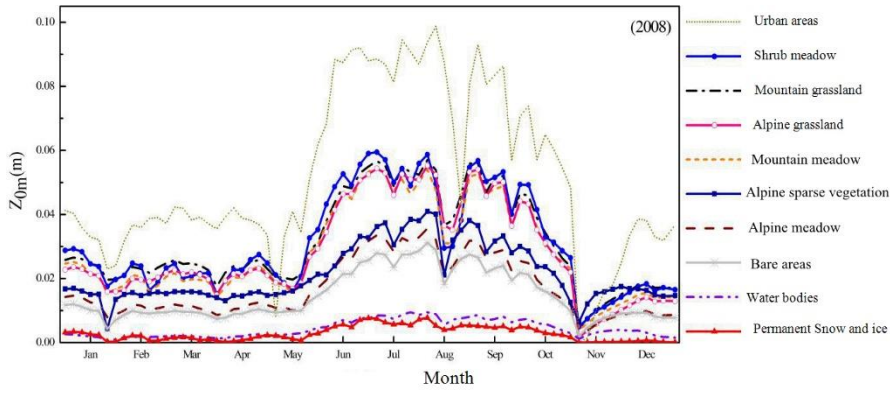
671
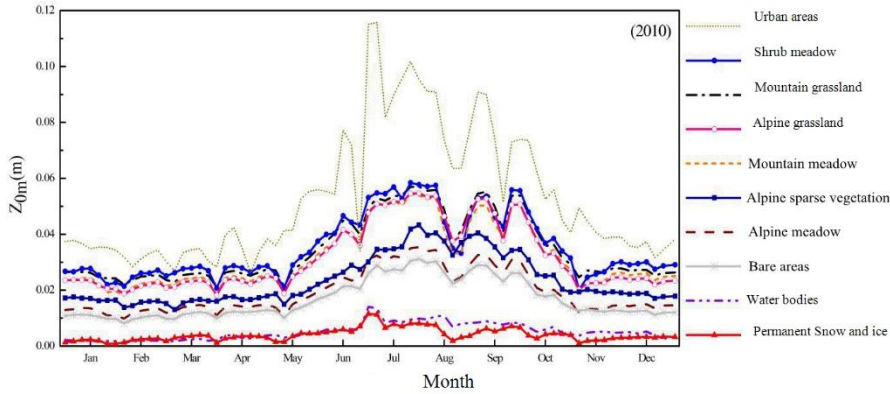
672
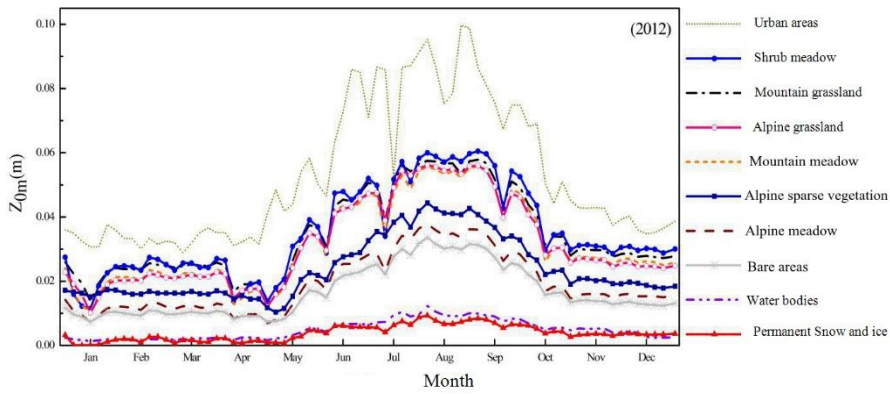
673
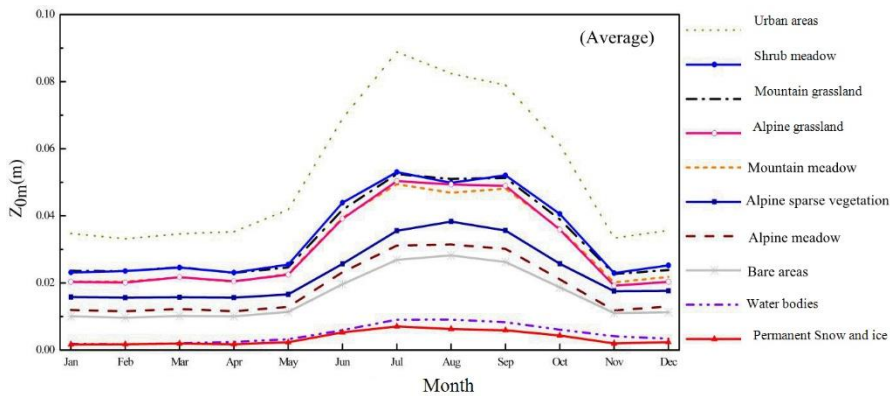
674

675 Fig. 8 Curve of the surface roughness length for different underlying surfaces

676

677 **(a)**

678

679 **(b)**

680
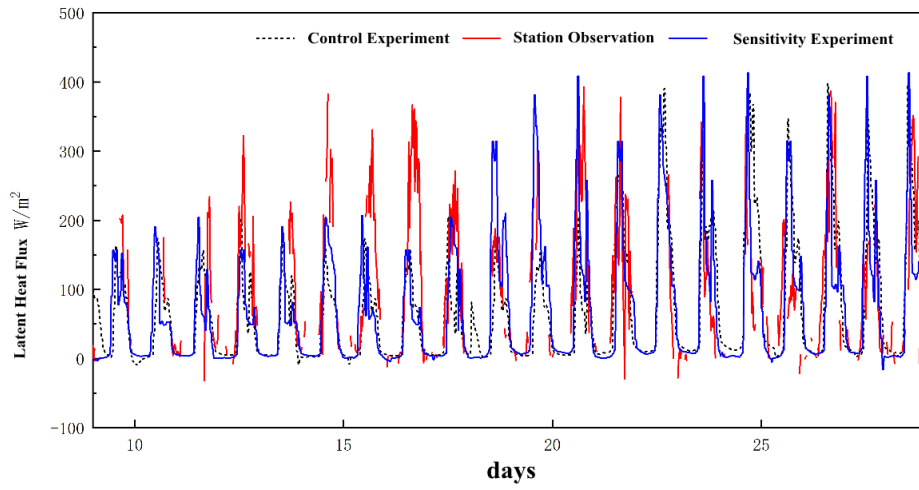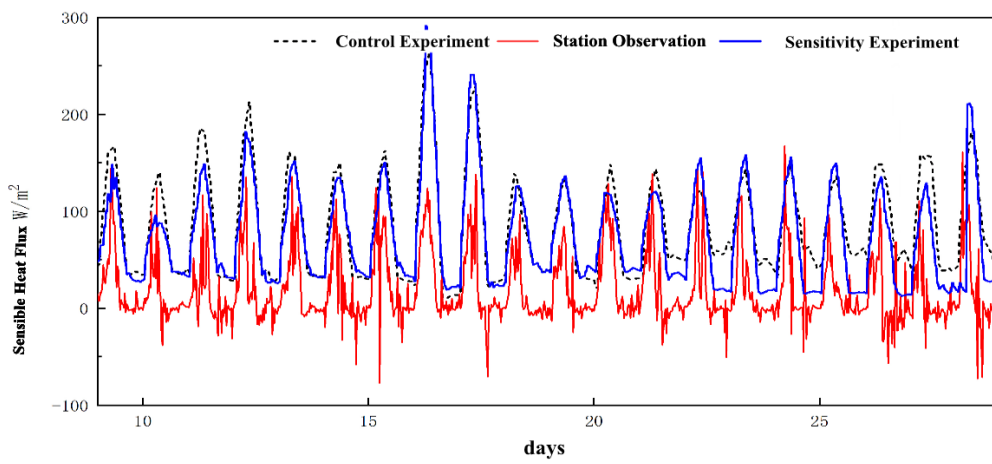
681   Figure 9 Comparison of simulated and observed sensible heat flux (a) and Comparison of

682   simulated and observed latent heat flux (b)

683
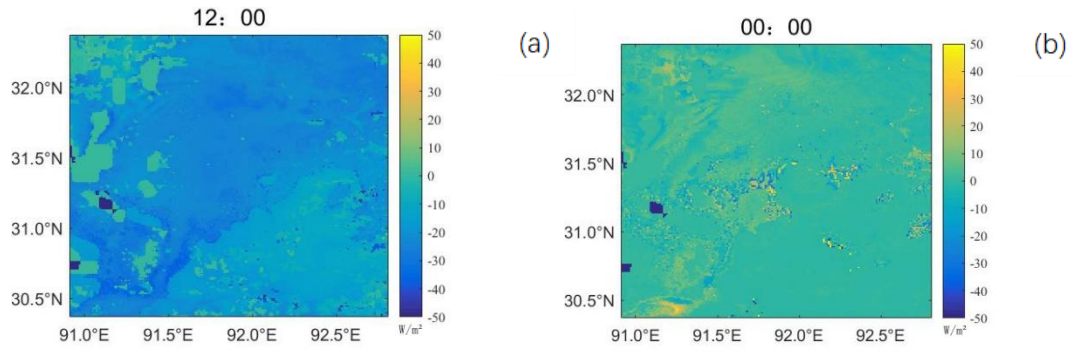
684

685
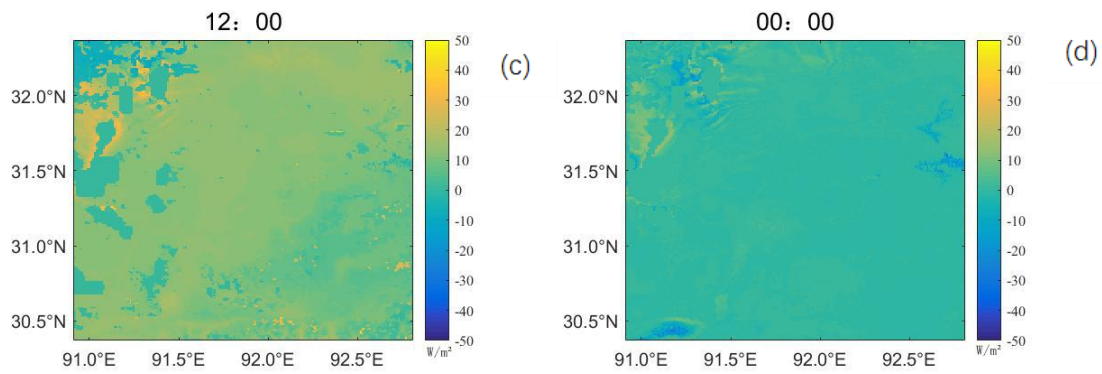
686

687 Figure 10 The difference of the control and sensitivity experiments simulated
688 regional sensible heat flux (a) 12:00, (b) 00:00 and latent heat flux (c) 12:00, (d)
689 00:00

690

691

692